Observations of the Evolution of the Nocturnal and Convective Boundary Layers and the Structure of Open-Celled Convection on 14 June 2002

LINDSAY J. BENNETT

School of Earth and Environment, University of Leeds, Leeds, United Kingdom

TAMMY M. WECKWERTH

National Center for Atmospheric Research, Earth Observing Laboratory, Boulder, Colorado*

ALAN M. BLYTH

National Centre for Atmospheric Science, University of Leeds, Leeds, United Kingdom

BART GEERTS AND QUN MIAO

Department of Atmospheric Science, University of Wyoming, Laramie, Wyoming

YVETTE P. RICHARDSON

Department of Meteorology, The Pennsylvania State University, University Park, Pennsylvania

(Manuscript received 19 August 2009, in final form 19 January 2010)

ABSTRACT

The Boundary Layer Evolution (BLE) missions of the International H_2O Project (IHOP_2002) were designed to provide comprehensive observations of the distribution of water vapor in the quiescent boundary layer and its evolution during the early morning. The case study discussed in this paper presents detailed observations of the development of the boundary layer from before sunrise through to the period of growth of the mature convective boundary layer (CBL) during the 14 June 2002 BLE mission. The large number of remote sensing platforms, including the multiple instruments collocated at the Homestead Profiling Site, provided a detailed set of measurements of the growth and structure of the CBL.

The observations describe the classic evolution of a daytime CBL, beginning with a shallow nocturnal boundary layer (NBL) below the remnants of the previous day's mixed layer, or residual layer. The vertical distribution of humidity in these layers during the early morning was affected by advection of dry air and by gravity waves. About an hour after sunrise a CBL developed, and gradually deepened with time as it mixed out the NBL and residual layer. The growth of the top of the CBL was particularly well observed because of the strong vertical gradients in temperature, humidity, and aerosol concentration. As the CBL deepened and the average CBL wind speed decreased, the mode of convective organization evolved from horizontal convective rolls to open-celled convection. A unique set of detailed measurements of the structure of the open cells was obtained from multiple instruments including the Doppler-on-Wheels radar, the Mobile Integrated Profiling System wind profiler, and the Scanning Raman lidar. They showed the relationship between open cells, thermals, mantle echoes, and the CBL top.

* The National Center for Atmospheric Research is sponsored by the National Science Foundation.

Corresponding author address: Lindsay J. Bennett, School of Earth and Environment, University of Leeds, Leeds LS2 9JT, United Kingdom.
E-mail: l.j.bennett@leeds.ac.uk

DOI: 10.1175/2010MWR3200.1

1. Introduction

The International H_2O Project (IHOP_2002) took place in the southern Great Plains in the summer of 2002 (Weckwerth et al. 2004). The boundary layer evolution (BLE) component aimed to better understand the distribution of water vapor in the quiescent boundary layer and its evolution from the early morning through the development of the daytime convective boundary layer (CBL). These missions are the first time the boundary layer has been studied with such a dense dataset.

The structure of the boundary layer over land during synoptic-scale high pressure conditions has a well-defined diurnal evolution and has been described in terms of the vertical profile of virtual potential temperature θ_v (Stull 1988) (Fig. 1). During the early morning, the stable nocturnal boundary layer (NBL), characterized by an increase of θ_v with height, occupies the lowest few hundred meters and is overlaid by a neutrally stratified residual layer (Fig. 1a). Shortly after sunrise thermals begin to form, which transport warm air from the surface upward and cause entrainment of warm air from above the nocturnal inversion into the NBL. This convective overturning leads to the gradual erosion of the stable layer (Garratt 1994; Angevine 2008). Mechanical turbulence generated by large wind shear in the NBL can also lead to mixing. Recent work has suggested that shear-driven turbulence plays a larger role than convective turbulence in the warming and destruction of the NBL (e.g., Angevine et al. 2001; Lapworth 2006). As the stable layer is mixed out, a shallow CBL (or mixed layer) develops at the surface, where θ_v is approximately constant with height (Fig. 1b). The new CBL grows through the residual layer as a result of entrainment and mixing until it reaches an overlying stable layer or capping inversion, which inhibits further vertical development (Figs. 1c,d).

There have been many observations of horizontal variability in humidity within the CBL due to thermals and horizontal convective rolls (e.g., Warner and Telford 1963, 1967; Crum et al. 1987; LeMone and Pennell 1976; Weckwerth et al. 1996). However, there have been few observations of the variability in humidity during the early morning prior to the formation of thermals and of the vertical and horizontal structure of the water vapor field during the transition from the NBL to the CBL. A common observation is the decrease of humidity with height in the convective boundary layer (e.g., Mahrt 1976; Crook 1996; Linne et al. 2007). It has been suggested that the vertical gradient is a result of entrainment of dry air at the top of the boundary layer outweighing the moistening by surface fluxes and the vertical transport of this moist air (Mahrt 1976). Mahrt (1991) suggested that

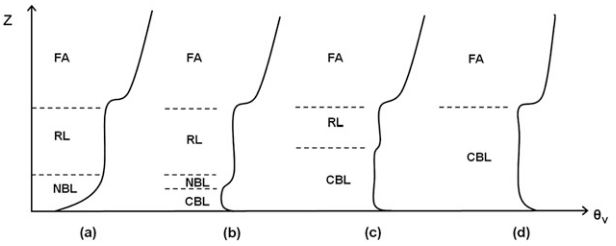

FIG. 1. Typical profiles of virtual potential temperature showing the evolution of the boundary layer during the diurnal cycle: (a) before sunrise, (b) early morning, (c) mid-to-late morning, and (d) afternoon. NBL and CBL defined in text; residual layer (RL), and free atmosphere (FA). Adapted from Fig. 1.12 of Stull (1988).

the diurnal evolution of the boundary layer could be characterized by two regimes. The moistening regime occurs during the early morning and is associated with large surface evaporation. The drying regime later in the morning is associated with entrainment at the top of the boundary layer after the NBL has been eliminated. For example, Grossman and Gamage (1995) observed a period of drying during the rapid growth of the CBL as it encountered an elevated mixed layer (EML). Penetrative convection caused the downward mixing of drier air from the EML. Horizontal advection can also play a large role in the humidity structure of the boundary layer (Mahrt 1976; LeMone et al. 2002).

The organization of boundary layer convection often occurs in the form of two-dimensional horizontal convective rolls (cloud streets) or three-dimensional cells and is frequently observed in satellite images, particularly over the oceans (Atkinson and Zhang 1996). Atkinson and Zhang (1996) presented a comprehensive review of mesoscale shallow convection and summarized the characteristics of rolls and cells. They concluded that in general rolls tend to occur in environments of moderate wind shear (1–10 m s^{-1} km^{-1}) whereas cellular convection usually occurs in a weakly sheared environment (less than 2 m s^{-1} km^{-1}). However, more recently, Weckwerth et al. (1999) investigated the evolution of rolls over land and showed that they formed in even minimal wind speed and shear conditions. They found that roll formation was controlled solely by the magnitude of the buoyancy flux. Roll dissipation was controlled by the convective instability of the boundary layer and its evolution into either open cells or unorganized random convection was controlled by the magnitude of the wind speed.

Over the oceans, open-celled convection is recognized by the honeycomb or hexagonal organization of the clouds, associated with ascending motion in a ring around the outside and descending motion in the center (Agee et al. 1973; Agee and Dowell 1974). The convection is

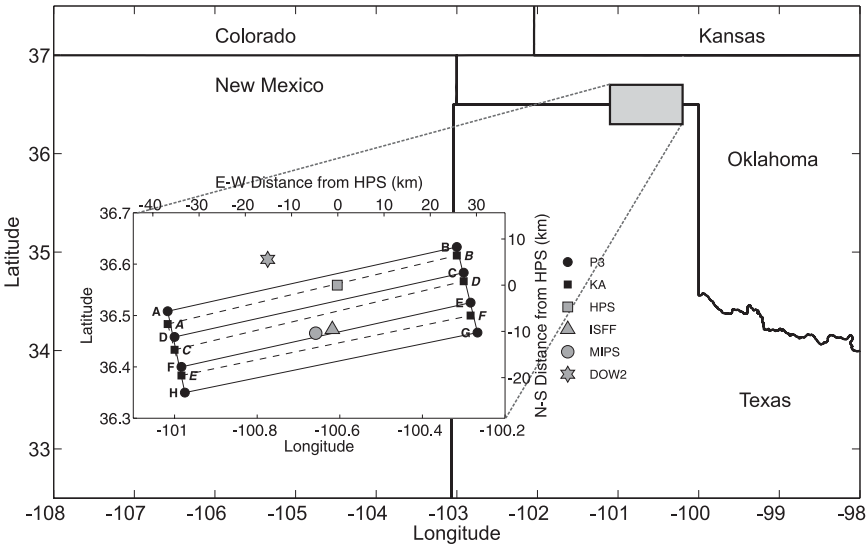

FIG. 2. Map showing the location of the instruments during the BLE mission on 14 Jun 2002.

driven by heating from below as cold air moves over relatively warm water. The average diameter and convective depth for open cells is 30 and 2 km, respectively. There have been few observations of open-celled convection over land similar to that seen over the oceans. However, several early radar studies investigating the development of the clear-air convective field over land reported similar hexagonal structures to those over the oceans, but on a much smaller scale (e.g., Hardy and Ottersten 1969; Konrad 1970). The cells observed by Hardy and Ottersten (1969) had diameters between 5 and 10 km with depths of 1–2 km and were detectable because of the scattering from insects within the updrafts of the thermals. The cells were composed of updrafts around the edges and downward motion in the center. The cells observed by Weckwerth et al. (1999) had diameters of ~2.4 km and those reported herein were 3 km on average.

This paper describes the development of the boundary layer over an essentially flat land surface from before sunrise to the time when it became a mature convective boundary layer, using a synthesis of datasets gathered with multiple instruments on 14 June 2002. The early morning boundary layer is characterized by a deep moist layer and oscillations associated with gravity waves. The growth phase of the convective boundary layer is characterized by the evolution from horizontal convective rolls to open cells. Simultaneous measurements from radars, lidars, and aircraft provide insight into the structure of the cells and in particular, the horizontal and vertical distribution of humidity. This is one of the few studies showing horizontal maps of the moisture in the CBL from an airborne water vapor lidar.

The structure of the paper is as follows. The layout and description of instrumentation are described in section 2 and the general meteorological situation in section 3. Observations of the evolution of the early morning boundary layer are presented in section 4, the development of the convective boundary layer in section 5, and the characteristics of the open cells in section 6. A summary of the observations are given in section 7. All times are in Central Standard Time (CST, UTC − 6 h), local solar noon was 1242 CST, and all heights are given as above ground level (AGL) unless otherwise stated.

2. Details of instrumentation

A map of the location of ground-based instrumentation and aircraft flight tracks on 14 June 2002 is shown in Fig. 2. The Homestead Profiling Site (HPS) accommodated the following instruments within 50–100 m of each other: the National Aeronautics and Space Administration Goddard Space Flight Center (NASA GSFC) Scanning Raman lidar (SRL) and Holographic Airborne Rotating Lidar Instrument Experiment (HARLIE), the University of Massachusetts Frequency Modulated-Continuous Wave (FMCW) radar, and the National Center for Atmospheric Research (NCAR) Integrated Sounding System (ISS).

a. Lidar

The SRL transmits light at a wavelength of λ = 354.7 nm and uses the ratio between the Raman-shifted return signals from water vapor (408 nm) and nitrogen (387 nm) to calculate the water vapor mixing ratio

(Whiteman et al. 1992; Whiteman and Melfi 1999). The SRL was operated in a vertically pointing mode and the raw data were sampled at 1-min intervals and with 30-m range gates. The raw data were smoothed to give a temporal resolution of 2 min and a spatial resolution of 60 m between 0 and 1 km and 100 m between 1 and 2 km.

The HARLIE transceiver employs a Holographic Optical Element to collimate and direct the outgoing laser beam, as well as to collect and focus the atmospheric backscatter, instead of a traditional telescope and scan mirror (Schwemmer 1998). The lidar scanned continuously at an elevation angle of 45° and rotation rate of $30° s^{-1}$, equivalent to a 12-s scan period. Aerosol backscatter profiles were obtained with a resolution of 20 m in height and at 100-ms intervals. Estimates of the height of the top of the boundary layer were calculated from the backscatter profiles, with an accuracy of ±20 m at 100-ms intervals.

The Naval Research Laboratory P3 aircraft was equipped with the Lidar pour l'Etude des Interactions Aérosols Nuages Dynamique Rayonnement et du Cycle de l'Eau (LEANDRE II), a water vapor differential absorption lidar (DIAL; Bruneau et al. 2001), which was operated in a horizontal-pointing configuration on 14 June 2002. The water vapor mixing ratio data used in this study were 5-s averages giving an along-track resolution of ~500 m and an along-beam resolution of 300 m.

b. Radar

The FMCW radar is an S-band (3 GHz) radar (Ince et al. 2003) that obtains profiles of reflectivity at 50-ms intervals and 2.5-m resolution up to an altitude of 2.5 km. The ISS Multiple Antenna Profiler (MAPR) is a 915-MHz wind profiler that uses the spaced antenna technique to provide profiles of boundary layer winds and backscatter. A second 915-MHz wind profiler belonging to the University of Alabama Mobile Integrated Profiling System (MIPS) was located 11 km to the south-southwest of the HPS (Knupp 2006). It measured horizontal and vertical winds and backscatter at 60–105-m vertical resolution and 1-min temporal resolution. The backscatter from these vertically pointing, lower-frequency radars is partly due to insects in the CBL (Rayleigh or Mie scattering) and partly due to turbulent fluctuations of the refractive index of air (Bragg scattering).

An X-band (9 GHz) Doppler-on-Wheels (DOW; Wurman et al. 1997) radar was located 16 km to the northwest of the HPS, measuring volume scans of reflectivity and radial velocity. The University of Wyoming King Air carried the 95-GHz Wyoming Cloud Radar (WCR), consisting of two antennas pointing vertically up and down simultaneously (Pazmany et al. 1994; Geerts and Miao 2005). At higher frequencies, especially 95 GHz, the backscatter is almost exclusively due to insects (Mie scattering).

c. Soundings and surface measurements

An Integrated Surface Flux Facility (ISFF) was deployed approximately 10 km to the south of the HPS and its measurements included fluxes of sensible and latent heat, radiation, and standard meteorological variables. The NCAR Tethered Atmospheric Observing System (TAOS) was deployed 1.6 km to the east of the HPS and consisted of up to 8 platforms tethered to a large balloon. Each platform had a Vaisala RS90 PTU package to measure pressure, temperature, and relative humidity; an R. M. Young propellor for wind speed; and a Honeywell magnetometer for wind direction. All data were sampled at 1 s, with accuracies of 5% for relative humidity, 0.5°C for temperature, and 1.5 hPa for pressure (Antikainen et al. 2002). Mixing ratio accuracy estimated from these values is $1 g kg^{-1}$. Serial radiosondes were launched at four stations, but only data from the ISS are used in this paper. The ISS system also used the Vaisala PTU package, but with additional GPS satellite navigation signals for wind measurements.

d. Aircraft

There were a total of six research aircraft during IHOP_2002, but only data from the P3 and the King Air are used in this paper. The P3 and King Air flew along the tracks shown in Fig. 2, at altitudes of approximately 1065 and 1225 m MSL. They were both equipped to make meteorological, turbulence, and cloud microphysical measurements. The accuracies of the pressure, temperature, and dewpoint temperature instruments are listed in online documentation for the Wyoming King Air as 0.5 mb, 0.5°C, and 1°C, respectively (http://flights.uwyo.edu/n2uw/users/KA_InstList.pdf), and for the P3 as 0.7 mb, 0.5°C, and 0.5°C (http://www.eol.ucar.edu/instrumentation/aircraft/C-130/documentation/c-130-investigator-handbook/c130handbook.chapter6_tables.1.pdf). Mixing ratio accuracies for the P3 and King Air are estimated from these values as 0.4 and $0.7 g kg^{-1}$, respectively.

3. General meteorological situation

On 14 June 2002, a ridge of high pressure was oriented north-northwest to south-southeast across the IHOP_2002 domain and there were no active convective systems or large-scale boundaries present. A band of stratocumulus clouds covered the southwest region of the domain during the early hours of the mission (Fig. 3a) but advected southward to leave a mostly cloud-free domain throughout the day (Fig. 3b). Pyranometer data from the MIPS surface station shows that solar radiation was

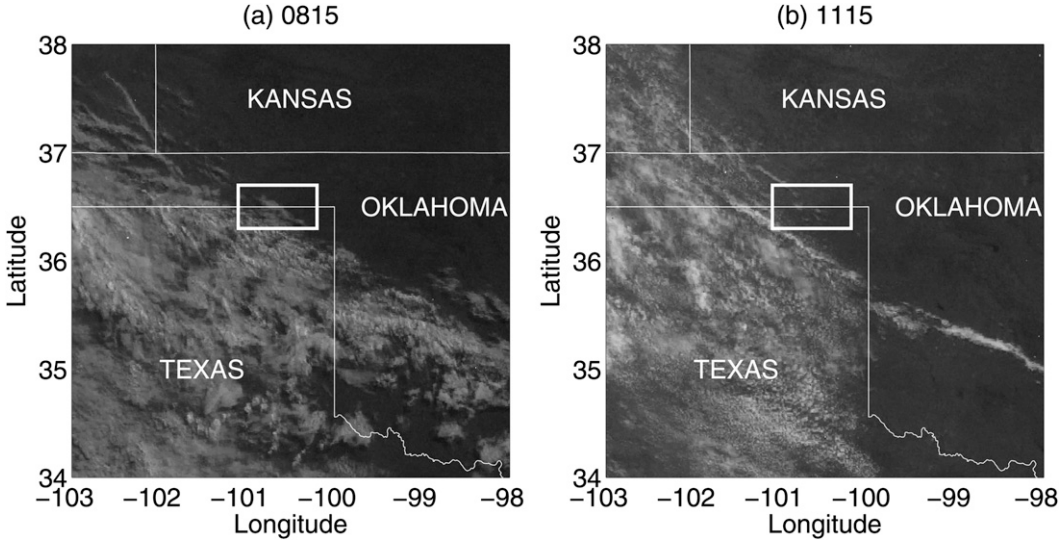

FIG. 3. *GOES-11* visible satellite imagery at (a) 0815 and (b) 1115 CST. The rectangle corresponds to the domain in Fig. 2.

intermittently reduced because of cloud cover during three periods: 0815–0855, 1110–1135, and 1300–1320 CST (Fig. 4a). The stratocumulus band and subsequent filaments to the north of the band were responsible for the reduction in radiation during the morning. A few very small cumulus clouds were visible in satellite images during the early afternoon.

The evolution of the wind profile is shown in Fig. 4b. Relatively strong (6–7 m s^{-1}) low-level northeasterly winds developed at 0630 CST, persisting until 0840 CST and then decreasing to ~2 m s^{-1} by 1000 CST. As the wind speed decreased the wind direction veered to the east, then to the southeast, and to the south by 1200 CST. The structure of the developing convective boundary layer (CBL) was influenced by the evolution of the winds. The winds aloft (1–1.5 km) were generally from the north or northeast, with a similar decrease from 7 to 2 m s^{-1} between 0400 and 1000 CST.

In situ measurements from the King Air and P3 illustrated the mesoscale variations in temperature and moisture across the domain during the morning between approximately 0545 and 1140 CST (not shown). The northern leg, AB (see Fig. 2), was cooler than the central and southern legs, CD and EF, respectively. Surface analyses showed that these variations were caused by cooler air advecting into the northeast of the domain during the morning between 0600 and 0900 CST (Couvreux et al. 2009).

There was also a large east–west gradient in humidity, which intensified with time. The humidity was greatest in the west and decreased gradually toward the east, in contrast to the climatological gradient that characterizes the Great Plains during the spring and summer months (Dodd 1965; Hoch and Markowski 2005). Couvreux et al. (2009) investigated the nature of this mesoscale gradient in humidity and found that it was a result of the distribution of precipitation from previous convective events, soil moisture content, and advection.

4. Evolution of the early morning boundary layer

The evolution of the early morning boundary layer on 14 June 2002 in the area around the HPS was observed in detail by a combination of sensors (Fig. 5). The height of the NBL is often difficult to define but is usually taken to be the top of the nocturnal inversion or the height of a low-level wind speed maximum (Mahrt 1979; Stull 1988). The 0415 CST sounding shows that the wind speed increased sharply in a shallow layer from the surface to approximately $z = 50$ m where it reached a maximum of 4.8 m s^{-1}. It then decreased with height up to 200 m. The maximum was similar at 0530 CST, but located at $z =$ 110 m. The increase of θ_v with height in this layer indicates the stability associated with the NBL. The figure shows that the water vapor mixing ratio q decreased with height within and above the NBL to minimum values at approximately $z = 120$ m at 0415 CST and 175 m at 0530 CST, then increased to maximum values at 230 and 330 m, respectively. This is in contrast to the profiles observed by Mahrt (1979) where q increased with height in the region of the low-level jet and then decreased rapidly above.

A deep moist layer ($q > 8$ g kg^{-1}) extended from the lowest range gate (315 m) of the SRL to an altitude of 1.1 km from the start of observations at 0415 CST until

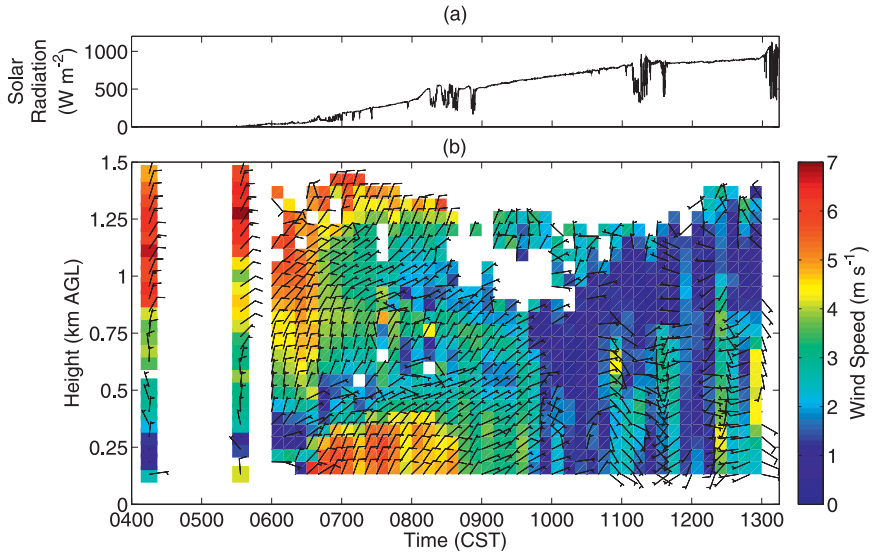

FIG. 4. (a) Pyranometer data from the MIPS surface station. (b) Time–height diagram of wind speed (colors) and wind barbs (black vectors) between 0400 and 1315 CST. The single profiles at 0414 and 0533 CST are from the ISS sounding at the Homestead site, less than 10 km distance from the location of the MIPS instruments.

just after sunrise at 0530 CST. This was probably a residual layer, connected with the previous day's mixed layer.

The magnitude and structure of the profile of q is consistent between the SRL and the radiosondes. Both datasets show that there was a gradual decrease in q with height through the residual layer from ~10 g kg^{-1} at $z = 300$ m to ~8 g kg^{-1} at 1 km and that it was embedded with several layers of relatively moister air. At 0415 CST, there were maxima in the radiosonde profile at $z = 230$, 500, and 710 m, but there was only one maximum in the SRL profile at 610 m. At 0530 CST, there were maxima in the radiosonde profile at $z = 330$ and 600 m and in the SRL profile at 390 and 670 m. These differences are expected because the radiosondes were not launched directly above the SRL and they drifted horizontally with the wind by typically 600 m during the first 800 m of ascent.

There was significant drying in the upper half of the residual layer from 0525 CST, coinciding with sunrise and a change in the wind direction from the north-northeast to the northeast (Fig. 4b), advecting drier air into the domain. The depth of the residual layer, determined from the sharp gradient in q from the SRL, decreased sharply from $z = 1.1$ km to approximately 0.7 km by 0530 CST. The mixing ratio decreased rapidly with height above 0.7 km before increasing again within a shallow elevated moist layer between 1.1 and 1.4 km. The elevated layer coincided with a region of higher wind speed, backing in the wind direction, and a stable layer.

The sensible heat flux became positive at 0615 CST, 50 min after sunrise (Fig. 5). Angevine et al. (2001) defined this time as the *crossover* and found it to occur on average 1.3 h after sunrise. The latent heat flux also began to increase rapidly at this time. The development of a CBL began soon after crossover, but its depth, z_i, is difficult to define because of the data gap below the minimum range of the SRL. However, there is an indication of the growth of the CBL from three point measurements: $z_i = 60$ m at 0702 CST measured by the WCR, 100 m at 0730 CST measured by the ISS sounding, and 394 m at 0815 CST observed as a sharp transition in the entire day's time series of vertical velocity from the P3. Angevine et al. (2001) defined the CBL *onset* to be the time when the nocturnal inversion has been eroded and found that the median onset time occurred 2.7 h after sunrise. In this case, the decrease of θ_v with height (Fig. 5) shows that the nocturnal inversion had been fully eroded by 0730 CST, 2 h after sunrise. It is possible that the strong surface winds added some mechanical mixing and enabled the faster erosion of the NBL.

During the early growth of the CBL from 0630 to 0830 CST the latent heat flux increased from 30 to 160 W m^{-2}. However, there was a decrease in q with time at all levels within the lowest 300 m. The ISS surface station measured a decrease in q from 11.2 to 10.5 g kg^{-1} and TAOS measured a decrease at $z = 100$ m from 10.6 to 9.3 g kg^{-1}. The drying is likely to be due to a combination of vertical transport of moisture by thermals, entrainment of drier air from above, and advection of drier air by the northeasterly flow. The remaining residual layer above the shallow CBL also experienced drying due to advection. The SRL measured a decrease in q from 9.8 to 9 g kg^{-1} at $z = 460$ m. The

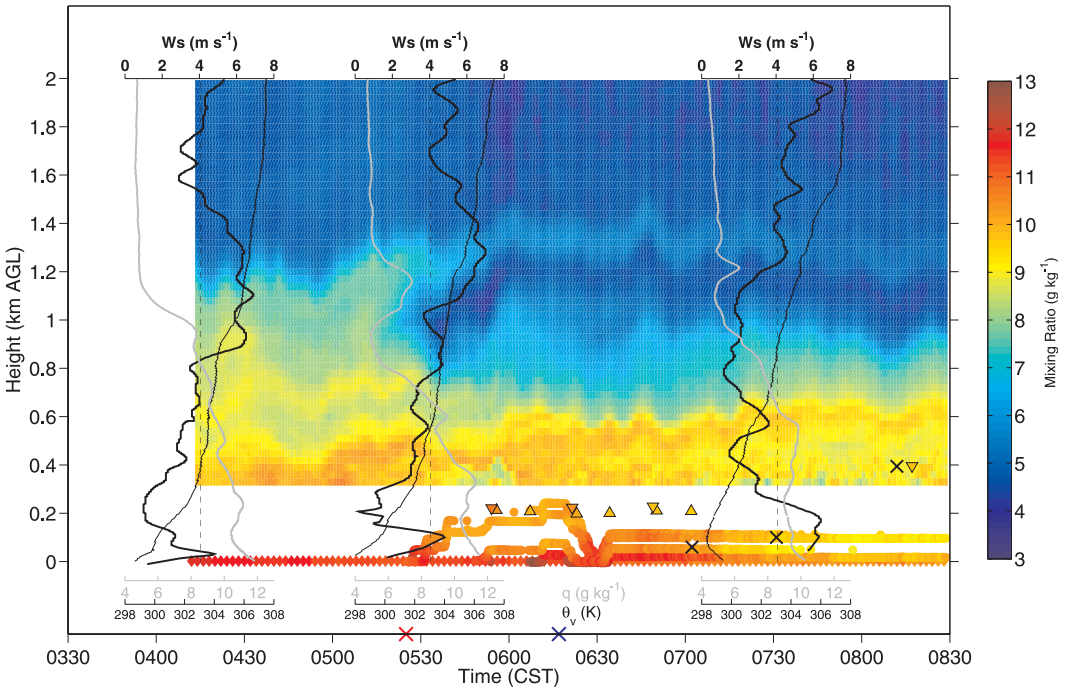

FIG. 5. Time–height diagram of mixing ratio from the SRL between 0415 and 0830 CST. Mixing ratio from the ISS surface station (diamonds), King Air and P3 aircraft (upward- and downward-pointing triangles, respectively), and TAOS (circles) is plotted below the minimum range of the SRL. The aircraft data are a 1-min-average value of mixing ratio measured for each pass over the HPS (equating to a distance of approximately 5 km). Vertical profiles of wind speed (Ws, thick black), mixing ratio (q, gray), and virtual potential temperature (θ_v, thin black) from the ISS soundings at 0415, 0530, and 0730 CST are also shown. The red cross corresponds to sunrise at 0525 CST and the blue cross corresponds to the time the sensible heat flux, measured by the ISFF, became positive. The black crosses indicate the early growth of the CBL, as described in text.

0730 CST sounding shows that q decreased with height from the surface to a minimum at approximately z = 230 m and then increased to a peak at the top of the residual layer at 600 m. This is in contrast to the mature CBL where the humidity usually decreases with height from the surface to the top of the CBL (Mahrt 1976), as will be shown for this case in section 5. The peak in q also coincided with a layer of enhanced wind speed.

Throughout the whole time period shown in Fig. 5 the vertical profile of humidity within the residual layer was also being perturbed by oscillations, which suggest the presence of gravity waves. The MIPS wind profiler observed similar structures during the same time period (Fig. 6). Several elevated layers of the increased signal-to-noise ratio (SNR) can be seen between 0545 and 0800 CST, the clearest ones being centered at altitudes of 0.5 and 0.8 km between 0545 and 0630 CST (Fig. 6a). Although it is difficult to distinguish individual peaks and troughs in the SNR field because of the lower resolution of the profiler than the SRL, the corresponding vertical velocity field reveals the oscillations very clearly (Fig. 6b). Alternating periods of upward and downward motion (maximum of +0.5 m s^{-1} and minimum of −0.4 m s^{-1}) can be seen from the first gate at 143 m to the maximum extent of the data at 1.5 km. Convective updrafts and downdrafts start to dominate the signal below 500 m from 0645 CST onward, but the gravity wave oscillations are still present at higher altitudes. The average period of oscillation between 0545 to 0800 CST estimated from the vertical velocity data is approximately 19 min, which equates to an average frequency of 8.6×10^{-4} Hz. The Scorer parameter (Lin 2007) was calculated using the frequency information and sounding data and the analysis showed that the atmosphere was conducive to gravity wave propagation.

5. Evolution of the convective boundary layer

The continued development of the CBL after it had eroded the NBL was observed simultaneously by multiple instruments at the HPS. Figure 7 shows the mixing ratio field between 0600 and 1300 CST from the SRL, TAOS, and ISS radiosondes. The additional lines and symbols represent the depth of the CBL derived from the MAPR, FMCW, HARLIE, WCR, ISS, and the SRL itself. The top of the CBL only becomes easily

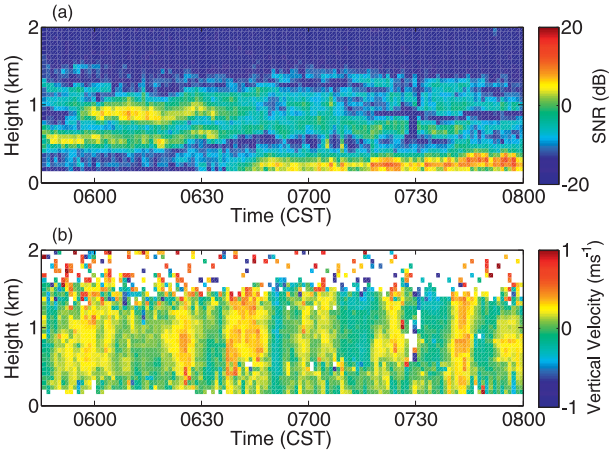

FIG. 6. MIPS wind profiler time–height diagrams of (a) signal-to-noise ratio and (b) vertical velocity from 0545 to 0800 CST.

discernible once it erodes through the residual layer at 0930 CST. It increases in altitude between 0930 and 1300 CST from approximately z = 750–1600 m, equating to a growth rate of 6.7 cm s^{-1}. This is comparable with other remote sensing observations of the growth of the CBL (e.g., Boers and Eloranta 1986; Angevine et al. 1994; Cohn and Angevine 2000). The growth is a result of entrainment of air above the CBL by overshooting thermals. Throughout this time period the SRL mixing ratio at the top of the CBL is characterized by alternating regions of moist domes and dry intrusions, which will be discussed further in section 6.

During the growth of the CBL between 0830 and 1300 CST, the humidity continued to decrease within the lowest 300 m AGL. The latent heat flux increased steadily from 160 W m^{-2} at 0830 CST to a peak of 250 W m^{-2} at 1145 CST, then leveled off at this value until it started decreasing an hour later. Advection of drier air was probably dominant until the wind veered to the southeast at 1100 CST. However, strong convective mixing and the vertical transport of moisture was probably the main mechanism for the drying at low levels between 1100 and 1300 CST. The SRL measured a decrease of mixing ratio with height throughout the CBL during this period as a result of entrainment of dry air at the top of the CBL, consistent with previous studies (e.g., Mahrt 1976; Crook 1996).

The magnitude of mixing ratio between the majority of overlapping datasets agrees to within 1 g kg^{-1}, which is within the range of accuracy of the instruments. It is unreasonable to expect any better agreement, particularly between the ground-based and airborne instruments, as they are not sampling the same volume of air because of the differences in time and space of the measurements.

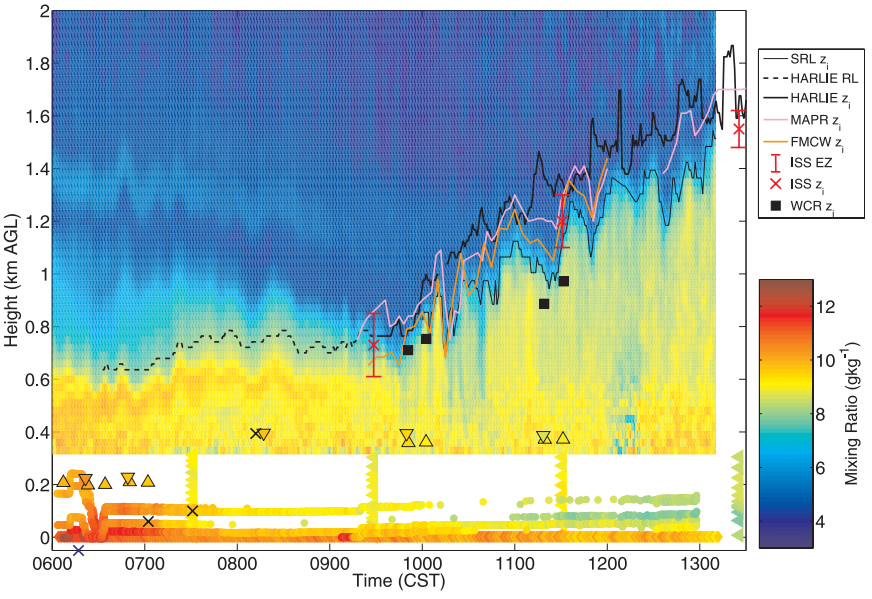

FIG. 7. Evolution of the moisture field between 0600 and 1300 CST and comparisons of boundary layer depth from multiple instruments. The symbols and colors are the same as in Fig. 5, but the ISS radiosonde mixing ratio is represented here by left-pointing triangles. The additional lines and markers represent the residual layer determined by HARLIE (dashed black), the CBL depth determined by the SRL (thin black), HARLIE (thick black), MAPR (pink), FMCW radar (orange), WCR (black squares) and ISS soundings (red crosses), and the entrainment zone determined from the ISS soundings (red error bars).

Quantitatively defining the top of the CBL has been the subject of much research since it is an important parameter in applications such as pollution dispersion modeling. Reviews of remote sensing methods to derive the CBL depth (or mixed layer height) can be found in Seibert et al. (2000) and Emeis et al. (2008), for example. The altitude of z_i, and the top and bottom of the entrainment zone, were estimated from profiles of θ_v from the ISS soundings, based on the definition given in Wyngaard and LeMone (1980) and Stull (1988). One-minute averages of z_i were determined from HARLIE aerosol backscatter profiles using an automated algorithm that employs the Haar wavelet technique documented by Davis et al. (2000). The algorithm finds the center of the aerosol gradient at the top of the CBL. The layer identified by the algorithm between altitudes of 0.6 and 0.8 km from 0600 to 0930 CST is not the CBL top, but corresponds with the top of the residual layer identified by the SRL. The maximum gradient in mixing ratio at the top of the CBL for each vertical profile of the SRL was used to construct its time series of z_i. The reflectivity data from MAPR and FMCW was much noisier; therefore, z_i was subjectively determined by estimating the peak in reflectivity every 5 min, based on the technique documented by Angevine et al. (1994). They suggested that the peak in SNR occurs just above the inversion base where the humidity gradients are strongest. The WCR value of z_i was derived from the reflectivity field using the method described in Geerts and Miao (2005) and Miao et al. (2006).

The average rate of growth of the CBL was comparable for all the instruments (Fig. 7). The time series of z_i from the SRL matched well with the instantaneous values determined from the radiosondes. The FMCW and MAPR mirrored the undulations in the SRL and although the absolute values of z_i were slightly lower, they were within the range of the entrainment zone, giving confidence in any one of the measurements. The HARLIE estimates of z_i were consistently higher than the SRL and the peaks and troughs did not correlate well with the other instruments. The main reason for the discrepancy is likely to be because the lidar scans at 45° elevation and the data are averaged over 360°. The WCR values of z_i are the lowest of all the instruments. The differences in absolute CBL height are mostly due to the sampling characteristics of the remote sensors, as well as the temporal resolution and the details of the algorithms used to define the CBL.

Continuous 1° elevation plan position indicator (PPI) scans from the DOW radar revealed a striking evolution of convective features throughout the morning and early afternoon (Fig. 8). The first clear-air signals were observed from 0700 CST, but they had no particular organization

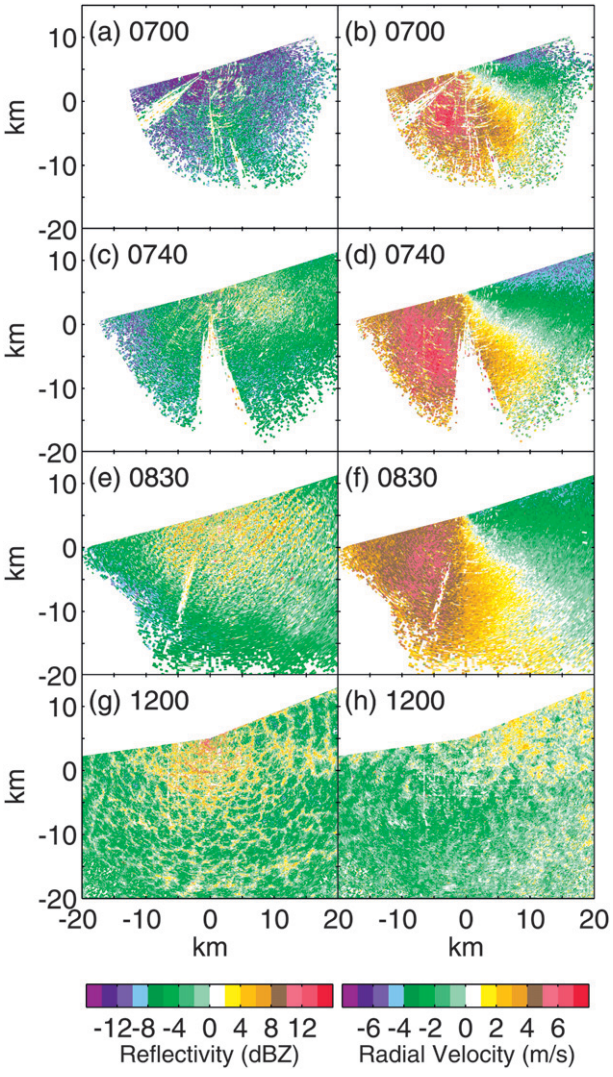

FIG. 8. Sequence of PPI scans at 1° elevation from the DOW radar with panels of (left) reflectivity and (right) radial velocity showing (a),(b) weak signals at 0700 CST; (c),(d) the first horizontal convective rolls at 0740 CST; (e),(f) well-developed rolls at 0830 CST; and (g),(h) open-celled convection at 1200 CST. The center of the radar beam reaches an altitude of 524 m at the 30-km range.

(Figs. 8a,b). The radar echoes developed into horizontal convective rolls 40 min later at 0740 CST (Figs. 8c,d). The rolls were most distinguishable at 0830 CST after increasing in spacing and size as the CBL depth increased (Figs. 8e,f). The rolls began to evolve into open-celled convection from 1000 CST, soon after the winds in the lowest 500 m had decreased to 2 m s^{-1} and veered to the east (Fig. 4b, section 3). The cells were particularly well defined by 1200 CST (Figs. 8g,h). This is consistent with previous observations of the development of the CBL, for example, those over Florida presented by Weckwerth et al. (1999). The undulations observed by the SRL at the

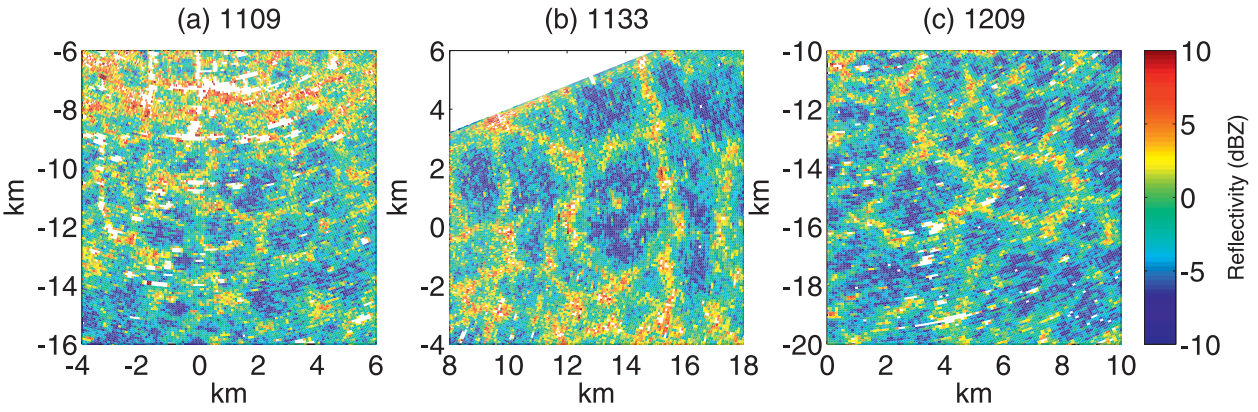

FIG. 9. One degree elevation PPI scans of DOW reflectivity illustrating various sizes of open-celled convection at (a) 1109, (b) 1133, and (c) 1209 CST.

top of the CBL and mirrored in the MAPR and FMCW time series of z_i between 1100 and 1300 CST (Fig. 7) are, for this case, a result of the open-celled organization of the CBL. The following section presents a unique insight into these cellular structures by comparing collocated measurements from the DOW radar, MIPS wind profiler, SRL, and aircraft.

6. Collocated measurements of open-celled convection

Examples of the open-celled convection observed by the DOW radar are shown in Fig. 9. The cells are hexagonal-shaped regions of high reflectivity surrounding a low reflectivity core. The high reflectivity is caused by large backscatter from insects that have been forced together by convergence and swept into the updraft branches of the cells (Wilson et al. 1994; Achtemeier 1991). Similarly, the low-reflectivity regions are associated with a broader region of downward motion causing the dispersion of insects. Cells existed with a variety of diameters, ranging from 2 to 4 km, comparable to other observations such as those of Konrad (1970) and Weckwerth et al. (1999). The examples in Fig. 9 illustrate a few well-defined cells; however, there was considerable variability in size and shape.

The MIPS wind profiler was located approximately 10 km east/16 km south of the DOW and 5 km west/10 km south of the ISS (Fig. 2). The wind profiler also observed structures associated with the open-celled convection (Fig. 10) as the cells advected with the main flow over the profiler. The top of the CBL was delineated by a layer of high SNR that slowly increased in height from an altitude of 0.7 km at 1000 CST to 0.9 km by 1100 CST and 1.1 km by 1215 CST. The rate of growth of the CBL was comparable to the other datasets shown in Fig. 7. Similarly, the increase was not linear, there were large variations associated with thermals within the cellular structures. The large backscatter was a result of the sharp gradient in humidity at the top of the CBL and the mixing between thermals and the environment (Angevine et al. 1994; White et al. 1991).

The inverted U-shaped echoes at 1115, 1127, 1139, and 1215 CST stand out very clearly and represent regions where this mixing is taking place. The minima in reflectivity below the echoes are due to the homogeneity in humidity within the cores of the thermals. Using the observed average wind speed at the altitude of the echoes (approximately 1–2 m s^{-1} between $z = 0.6$ and 1.1 km, Fig. 4b) and the time taken for the features to pass over the instrument (~13 min, assuming a steady state), their widths were between 800 and 1600 m. Such echoes, of comparable scales, were first observed by backscatter radars over 40 years ago in the CBL (Hardy and Ottersten 1969; Konrad 1970), and within cumulus clouds (Harper et al. 1957) where they were termed ''mantle echoes.''

Collocated data from the wind profiler and the DOW radar are presented in Fig. 11 to show that the mantle echoes were associated with the updraft branches of the open-celled convection. The mantle echoes at 1115, 1127, and 1139 CST were all associated with updrafts (black contours) that started at the lowest level of the

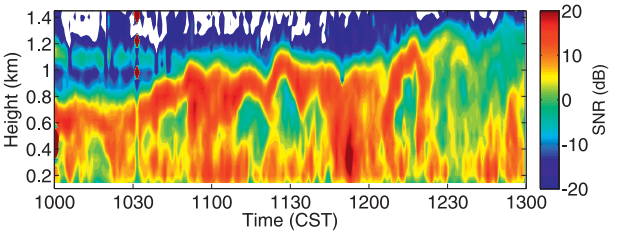

FIG. 10. Time–height diagram of SNR measured by the MIPS wind profiler between 1000 and 1300 CST.

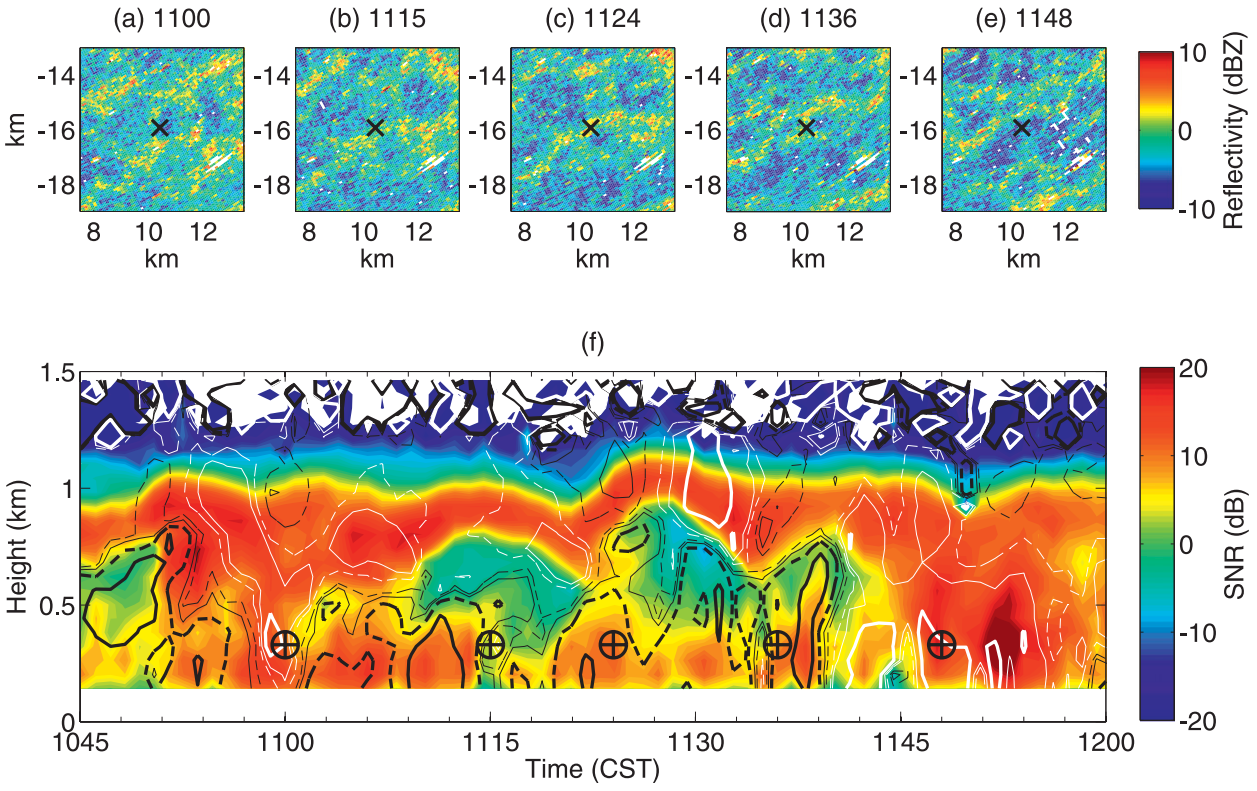

FIG. 11. One degree elevation PPI scans of DOW reflectivity for a 6 km^2 region centered on the MIPS wind profiler (black cross) at (a) 1100, (b) 1115, (c) 1124, (d) 1136, and (e) 1148 CST. (f) SNR measured by the wind profiler between 1045 and 1200 CST overlaid with contours of vertical velocity. The thin dashed, thin solid, thick dashed, and thick solid lines correspond to ±0.25, 0.5, 1, and 2 m s^{-1}, respectively, where black is positive and white is negative. The altitude of the DOW beam at the range of the wind profiler was approximately 330 m, represented by the cross-hair symbols.

wind profiler data (~200 m) and extended into the low SNR region beneath the top part of the echoes (Fig. 11f). Most of the updrafts extended upward all the way to the underside of the echoes. The echo at 1127 CST consisted of two updraft cores. The corresponding DOW scans show that the wind profiler was located in a region of high reflectivity corresponding to the edge of one of the open cells (Figs. 11b–d). It remained within the updraft branch of the cell as the cell advected toward the northeast.

Columns of high SNR extend from approximately 200 to 500 m within the updrafts. It is likely that these signals were dominated by Rayleigh scattering associated with plumes of insects being transported vertically by the updrafts, similar to the measurements of the WCR. Bragg scattering is unlikely because these are solid signals without minima at their centers like the mantle echoes. The humidity of the thermals was probably still quite homogeneous at these lower altitudes.

The updrafts were estimated to be between 540 and 900 m in width, using a wind speed range of 1.5–2.5 m s^{-1} (Fig. 4b) and a time to pass over the wind profiler of approximately 6 min. The mean width of the updraft plumes, calculated from the WCR using the method described in Miao et al. (2006), was found to be $0.34z_i$ and largely independent of height. Using the CBL depth of z_i = 1 km at this time gives smaller updraft widths of 340 m. The wind profiler widths are likely to be slightly overestimated because of the assumption made in the calculations and the lower resolution of the instrument compared with the WCR.

The wind profiler observed a broad region of downdraft between 1139 and 1200 CST, which was associated with high SNR throughout the whole depth of the CBL (Fig. 11f). The high SNR is most likely caused by Bragg scatter resulting from inhomogeneities in the refractive index of the descending air. The wind profiler was located under a low DOW reflectivity region within an open cell at this time (Fig. 11e). As the cell advected toward the northeast, the wind profiler remained under the low-reflectivity region. Conversely, the downdraft observed at 1100 CST was only a very narrow feature below z = 500 m and was surrounded by updrafts on either side (Fig. 11f). The wind profiler was located beneath

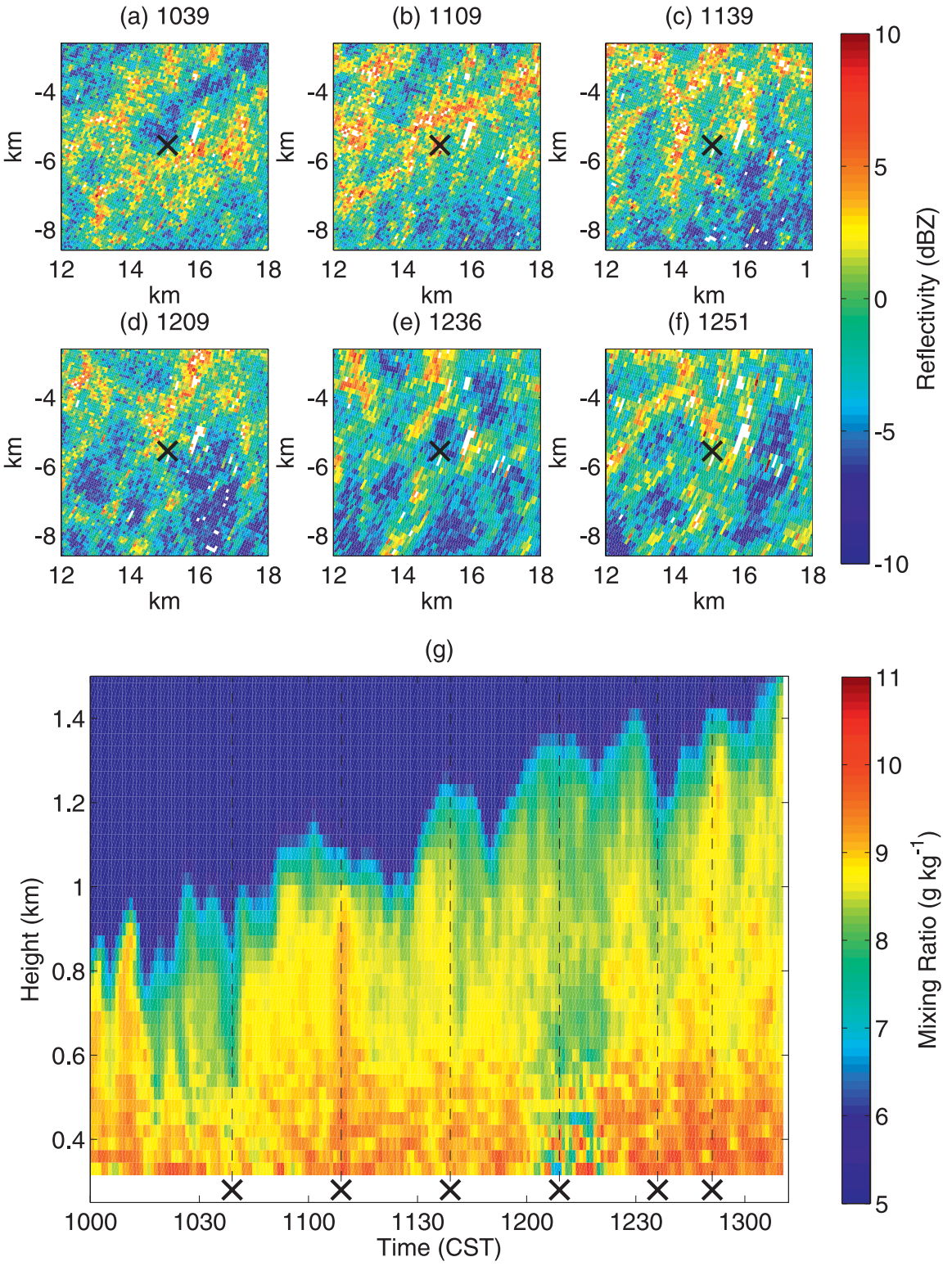

FIG. 12. One degree elevation PPI scans of DOW reflectivity for a 6 km^2 region centered on the SRL (black cross) at (a) 1039, (b) 1109, (c) 1139, (d) 1209, (e) 1236, and (f) 1251 CST. (g) Mixing ratio measured by the SRL between 1000 and 1312 CST. The dashed lines correspond to the time of the DOW scans in (a)–(f). The altitude of the center of the DOW beam at the range of the SRL was 280 m, represented by the crosses.

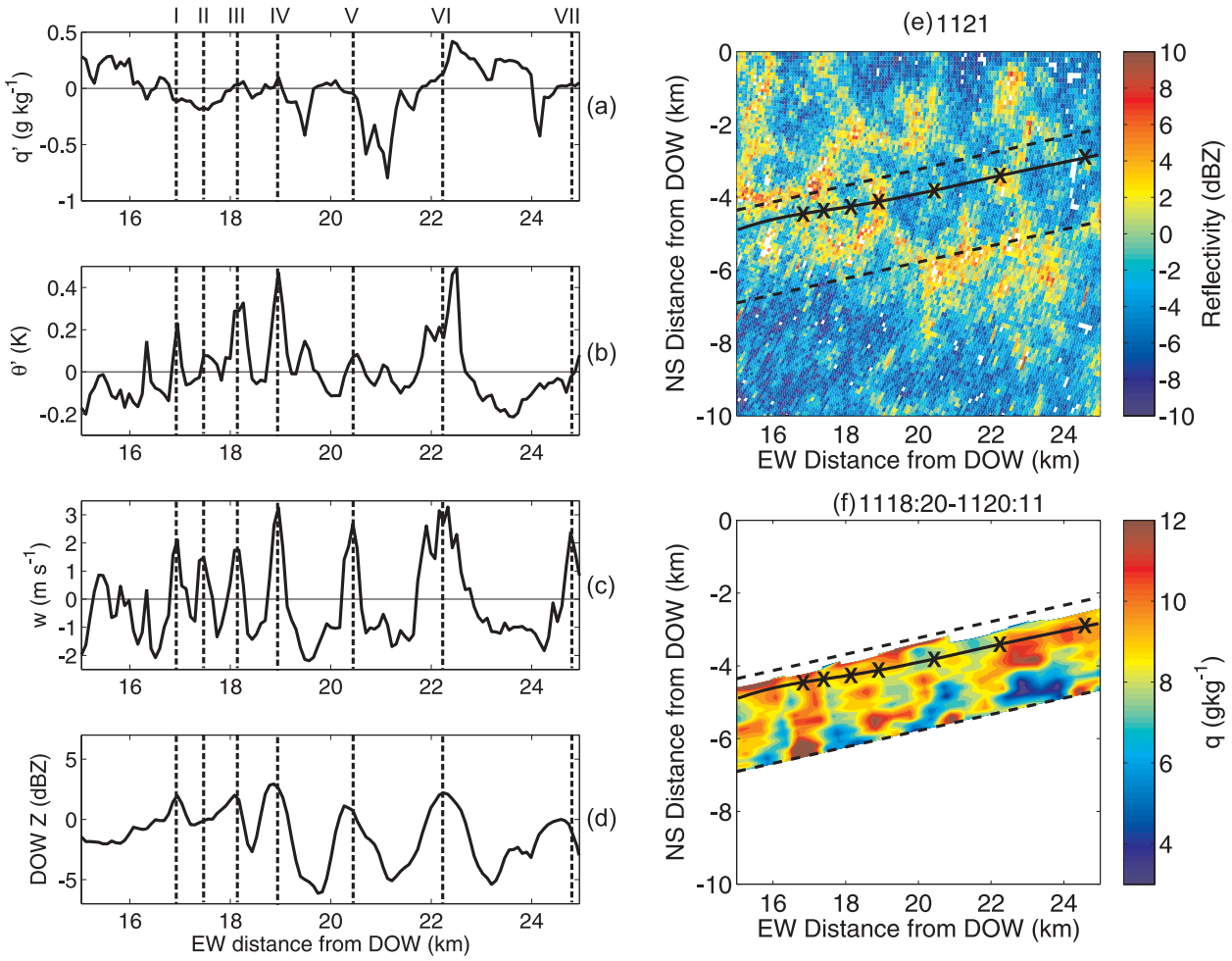

FIG. 13. Time series of (a) q' and (b) θ' (fluctuations from a 10-km running mean), and (c) w from the King Air between 1119:18 and 1121:12 CST. The King Air was flying from west to east along leg AB, at approximately 1234 m MSL, equivalent to 425 m AGL at the eastern end and 335 m AGL at the western end. (d) Time series of reflectivity extracted from the corresponding 1° elevation DOW PPI scan along the King Air track. The altitude of the DOW beam was an average of 356 m along the track. (e) The DOW scan is shown overlaid with the King Air track (solid black line) and the location of the LEANDRE II moisture field [dashed black lines, corresponding to (f)]. The labels I to VII correspond to the times of the main updrafts discussed in text.

the boundary between the high and low DOW reflectivity regions (Fig. 11a). A series of DOW images helped to clarify that as the cell moved to the northeast the wind profiler was only briefly within the downdraft region. The downdrafts were stronger toward lower altitudes and were strongest below 400 m.

Large variations in the humidity structure of the CBL were measured by the SRL during the time of open-celled convection. Collocated data from the SRL and the DOW radar are shown in Fig. 12. The top of the CBL was characterized by domelike structures of high humidity separated by narrower regions of drier air. The domes are similar in shape to the mantle echoes seen by the wind profiler (Fig. 11); however, they are much broader. Their widths are estimated to be between approximately 3 and 4.5 km, using a wind speed range of 2–3 m s^{-1} at the top of the CBL (measured by ISS radiosondes) and a time period of 25 min. It is also possible to distinguish a finer-scale structure to the domes themselves, where there are alternating thin columns of higher humidity and drier air. The moist columns are likely to be associated with individual thermals.

The SRL observed a narrow intrusion of dry air at 1039 CST when it was located under a boundary between high and low DOW reflectivity (Figs. 12a,g). Similarly a decrease in the height of the CBL and a zone of drier air was observed at 1236 CST, while the SRL was located under a low reflectivity region (Figs. 12e,g). At 1109 and 1251 CST, the SRL observed narrow moist columns of air that extended from 300 m to almost the

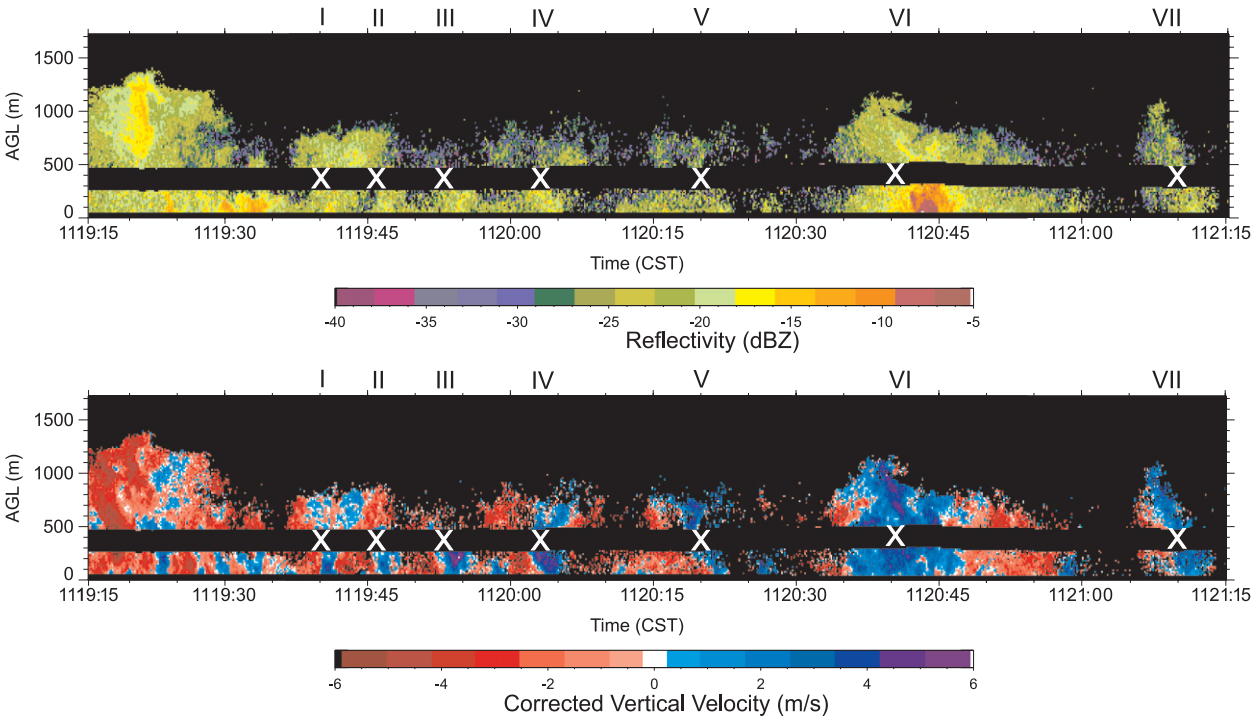

FIG. 14. Transects of (top) reflectivity and (bottom) vertical velocity from the WCR corresponding to the time period shown in Fig. 13. The white crosses and labels correspond to the same locations as the updrafts in Fig. 13.

top of the CBL. The SRL was located under regions of high reflectivity at the time (Figs. 12b,f). Similarly, the domes of humidity at 1139 and 1209 CST also corresponded to relatively higher zones of reflectivity (Figs. 12c,d,g). It is interesting that the open-cell organization observed by the radar in the lowest few hundred meters of the CBL corresponds so well with the features observed by the SRL at the top of the CBL. The humidity domes correspond to the updraft branches of the cells, where thermals transport moist air upward and the regions between the domes correspond to downdraft zones within the cells where the convective motions entrain drier air down into the CBL.

In situ measurements of q', θ', and w from the King Air and reflectivity from the DOW radar are shown in Figs. 13a–d. Seven updrafts, labeled I to VII, were observed during this transect. Most of them were associated with positive fluctuations in θ confirming that these features were thermals, transporting warm air upward. Most of the updrafts correspond to a region of enhanced reflectivity associated with the edges of the open-celled convection (Fig. 13e). The sequence of updrafts and downdrafts between 19 and 25 km east of the DOW is particularly distinct. The updrafts correspond to the edges of cells and the downdrafts correspond to the low reflectivity center of the cells. The updrafts are not strongly correlated with q', although there is an indication of relative maxima at some of these times. The variations in q' are generally broader than those in θ' and w, which may explain the weaker correlation. There is a stronger correlation between q' and w in the downdraft zones, representing the entrainment of dry air into the CBL.

Mixing ratio from LEANDRE II is shown in Fig. 13f. Despite the restricted range and reduced resolution of LEANDRE II compared to the DOW radar and King Air in situ measurements, the horizontal moisture fields show variations that may be associated with the open cells. The regions of high and low humidity are in approximately the same location as the regions of high and low reflectivity, respectively, but are sometimes broader. For example, the minimum in q located between $x = 22$ to 24 km and $y = -5$ to -4 km corresponds to an area of low reflectivity. Similarly, the maximum in q close to updraft V and the minima in q on either side correspond to maxima and minima in reflectivity.

Transects of reflectivity and vertical velocity from the WCR for the same time period are shown in Fig. 14. The WCR echoes, like those from the DOW radar, are due to scattering from insects. Geerts and Miao (2005) and Miao et al. (2006) showed that the plumes of high reflectivity correspond to the vertical displacement of the insects by thermal updrafts. The velocity field reveals the vertical motions associated with updrafts and downdrafts. The WCR reflectivity plumes correspond to the regions

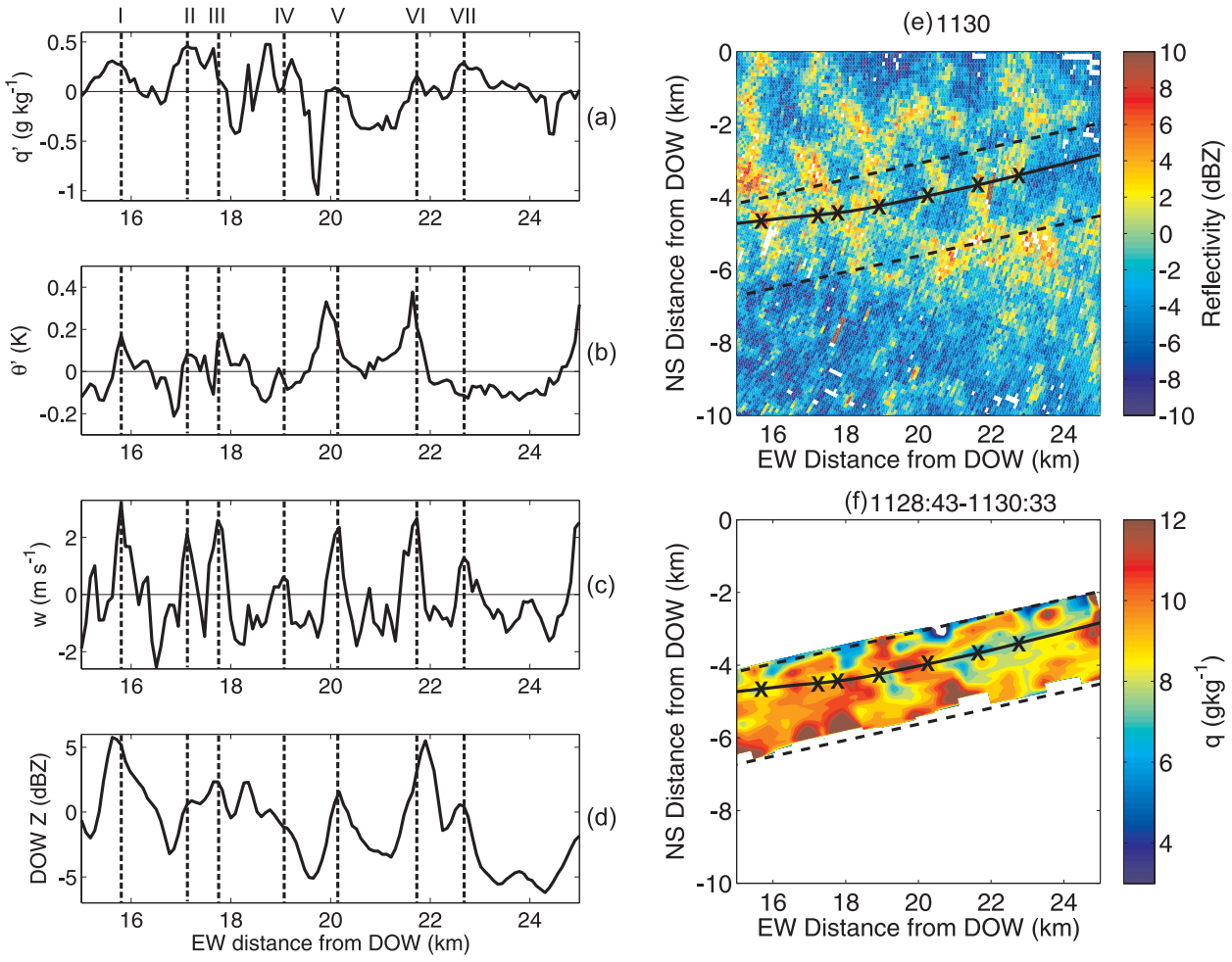

FIG. 15. As in Fig. 13, but for the return journey (east–west) along leg AB between 1129:29 and 1131:24 CST.

of enhanced DOW reflectivity. Both the in situ measurements and the WCR show that updrafts I to V were narrow whereas updraft VI was much broader. The WCR shows this broad updraft existed over the whole depth of the cell (Fig. 14). The center of the cells correspond to areas of depressed CBL height and very few insects, indicative of subsidence.

A second set of collocated King Air and DOW radar observations are shown in Fig. 15. Updrafts I, II, and III correspond to positive fluctuations in θ and q and enhanced values of DOW reflectivity. The θ fluctuations were similar widths to the updrafts (~500 m); however, the q fluctuations were generally broader than the updrafts (~1 km) as in Fig. 13. These observations correspond well with the LES simulations performed by Couvreux et al. (2005) for this case. They found that the CBL was characterized by larger scales for water vapor than for potential temperature and vertical velocity. One possible mechanism is the detrainment of moisture as thermals ascend in the CBL, similar to the process around cumulus clouds described by Perry and Hobbs (1996).

The reflectivity structures observed by the DOW radar were more unorganized at this time. Similarly, the corresponding reflectivity and velocity plumes observed by the WCR were inhomogeneous in both the horizontal and vertical (Fig. 16). More distinct cellular structures were observed along the second half of the transect. Updrafts IV and VI were clearly associated with the north–south-oriented edges of a hexagonal-like cell, large θ', and relative maxima in q'. This larger cell consisted of smaller structures and updraft V corresponds to the edge of one of these features. Updraft VII is associated with a separate area of high reflectivity to the east of the large cell.

A narrow region of dry air was observed at 19.7 km east of the DOW (Fig. 15a), adjacent to updraft V. It corresponded to a region of low reflectivity in the DOW data, a downdraft of -1.4 m s^{-1}, and a θ' value of $+0.2$ K. The WCR observed a narrow reflectivity and

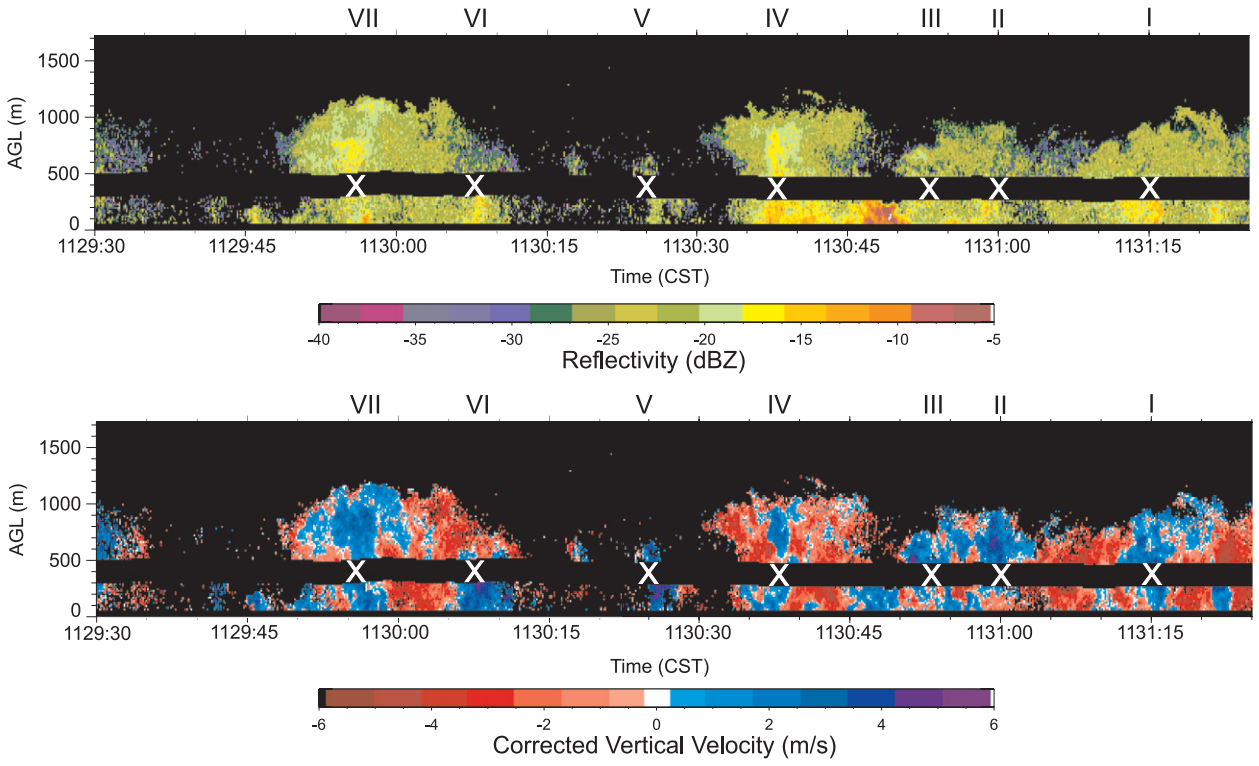

FIG. 16. As in Fig. 14, but for the return journey along leg AB.

strong velocity echo associated with updraft V, followed by a region with only a few weak echoes and downward motion (Fig. 16). Couvreux et al. (2005, 2007) showed that in the middle of the boundary layer vertical velocity was positively skewed, representing a few strong and narrow thermals. However, the distribution of humidity was negatively skewed, reflecting the presence of narrow intrusions of dry air, which they termed dry tongues. The dry tongues are caused by moist thermals penetrating into the overlying inversion (entrainment zone) and then sinking back down, pulling dry air down with them into the boundary layer. The dry intrusion observed by the King Air is an example of one of these dry tongues.

The horizontal moisture field from LEANDRE II is shown in Fig. 15f. There is a weaker correlation between the moisture and reflectivity fields for this section; however, there is still an indication that the lidar is able to resolve water vapor variability on the scale of the open cells.

The results in this section are summarized in the schematic diagram shown in Fig. 17. The open cells are characterized by high DOW reflectivity branches around their edges and low DOW reflectivity centers (feature 1). The long axis of the cell edges consist of multiple thermals carrying warm, moist air upward. However, it is not clear how many thermals span the short axis (i.e., the width) of the cell edges. The hexagonal shape of the cells is idealized and there were no instances where the instruments observed a cell edge directly along its short axis. The updrafts measured by the King Air and the MIPS wind profiler were 500–900 m wide (feature 2, solid lines), but the humidity field measured by the King Air was broader, on the order of 1 km (feature 2, dashed lines). Along the open cell edges, at the top of the CBL the thermals overshoot the capping inversion and entrain air down into the CBL. The entrainment and mixing of environmental air with the air inside the thermals results in the mantle echoes observed by the MIPS wind profiler (feature 3). The mantle echoes were larger than the thermals, having widths of 800–1600 m. The edges of the open cells were also collocated with dome-shaped structures of higher humidity at the top of the CBL, with scales of 3–5 km (feature 4). It appears that the domes are accumulations of several columns of higher humidity from individual thermals.

7. Summary

There have been few documented observations of the variability in humidity during the early morning and of the vertical and horizontal structure during the transition from the NBL to the CBL. This case study on 14 June 2002

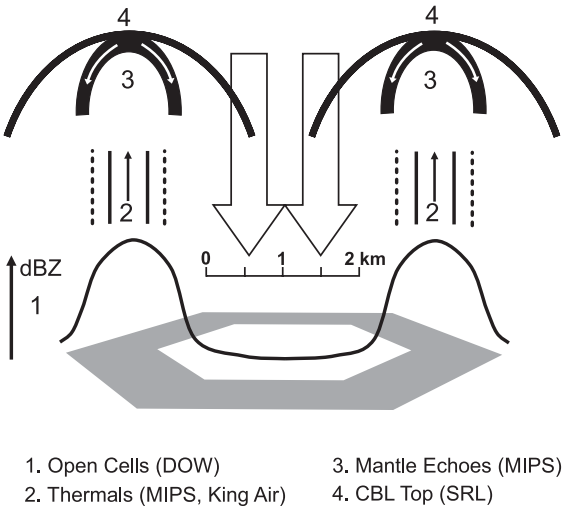

FIG. 17. Schematic representation of the structures associated with the open-celled convection. The shaded hexagon represents an idealized open cell observed by the DOW. Features 1–4 represent the structures observed by the DOW, King Air, MIPS wind profiler, and SRL, respectively. The arrows represent updrafts and downdrafts.

utilized simultaneous measurements from a large number of ground-based and airborne instruments to build a comprehensive picture of the evolution of the boundary layer, from shortly before sunrise through to the early afternoon. In particular the observations describe the vertical and horizontal distribution of humidity within the NBL and residual layer, and during the growth of the CBL.

The boundary layer observed on this day largely followed the classic diurnal evolution described by Stull (1988) and Garratt (1994). During the early morning there was a shallow NBL, and a deep moist residual layer that persisted for several hours before it became engulfed by the deepening CBL (Fig. 5). Advection of drier air into the region resulted in a minimum in the humidity profile in the middle of the residual layer and a peak at the top of the layer. Throughout the morning, the NBL and residual layer were perturbed by gravity waves, observed most clearly by the SRL, but they did not appear to have any affect on the development of the CBL.

A CBL started to develop about an hour after sunrise, but its growth was not well observed until it had mixed out the residual layer. After this time, the top of the CBL was clearly distinguishable because of the sharp gradient in temperature, humidity, and aerosol concentration separating the CBL from the free atmosphere (Fig. 7). Measurements of the altitude of the growing CBL by several different instruments were compared. There was a good correspondence between the average rates of growth compared with previous reported observations. Differences in the absolute altitudes of the CBL could mostly be explained by the different sampling characteristics of the instruments.

During the late morning and early afternoon, humidity in the CBL gradually decreased because of a combination of advection and mixing. There was a decrease in humidity with height, consistent with previous findings, but in contrast to the profile observed in the residual layer earlier in the morning. There were also significant horizontal variations in humidity. The SRL observed columns of higher humidity extending over a large fraction of the CBL associated with thermals. These were interspersed with intrusions of drier air. The King Air measurements showed that the humidity structures associated with thermals were broader than the widths of the updrafts, consistent with the modeling studies of Couvreux et al. (2005).

The organization of the CBL evolved from horizontal convective rolls into open-celled convection. Collocated measurements from the DOW radar, MIPS wind profiler, and SRL enabled a detailed analysis of the structure of the open cells. This is the first time the relationship between thermals, mantle echoes, CBL top, and open cells has been investigated. The results, summarized in Fig. 17, showed that the high reflectivity branches were associated with thermals transporting warm, moist air upward and the low-reflectivity centers were associated with drier, descending air. The reflectivity structures observed by the DOW radar in the lowest few hundred meters appear to be connected to the thermal processes and the humidity structures throughout the depth of the CBL.

The evolution of the thermal structures as they ascend in the CBL is not investigated in this paper. It is not clear why the humidity field of thermals is broader than the vertical velocity and temperature fields. A detrainment mechanism similar to that observed in cumulus clouds (Perry and Hobbs 1996) may be responsible. This is one of the most comprehensive datasets of open-celled convection over land. It would be interesting to further investigate whether such clear-air convective patterns may lead to deep moist convection, as sometimes observed for horizontal convective rolls (e.g., Weckwerth et al. 1996; Weckwerth 2000). Numerical simulations would aid in addressing these outstanding questions, as well as detailed analyses of two other BLE missions on 21 and 25 June during IHOP_2002.

Acknowledgments. We thank Kevin Knupp and two anonymous reviewers for their helpful suggestions, which improved the clarity and content of the manuscript. We are very grateful to all IHOP_2002 participants who collected data during the campaign. We thank

Geary Schwemmer (NASA GSFC), Dave Whiteman (NASA GSFC), Belay Demoz (NASA GSFC), and David Miller (PSU) for the supply of SRL and HARLIE data; Stephen Frasier (UMASS) for the FMCW data; Cyrille Flamant (CNRS) for the LEANDRE II data; and Bill Brown (NCAR/EOL) for the MAPR data. Those above along with Peggy LeMone (NCAR/MMM), Jim Wilson (NCAR/EOL/RAL), Daran Rife (NCAR/RAL), Christoph Kiemle (DLR), Wayne Angevine (NOAA), and Doug Parker (University of Leeds) provided stimulating discussions on this work. The first author was supported by the NERC Grants NER/S/A/2003/11275 and NE/E018483/1, and EOL/NCAR visitor funds. Funding from the NCAR/STEP program (TM) and the NSF Grants AGS-0849225 (BG and QM) and AGS-0638512 (YR) are also gratefully acknowledged.

REFERENCES

Achtemeier, G. L., 1991: The use of insects as tracers for ''clear-air'' boundary-layer studies by Doppler radar. *J. Atmos. Oceanic Technol.,* **8,** 746–765.

Agee, E. M., and K. E. Dowell, 1974: Observational studies of mesoscale cellular convection. *J. Appl. Meteor.,* **13,** 46–53.

——, T. S. Chen, and K. E. Dowell, 1973: A review of mesoscale cellular convection. *Bull. Amer. Meteor. Soc.,* **54,** 1004–1012.

Angevine, W. M., 2008: Transitional, entraining, cloudy, and coastal boundary layers. *Acta Geophys.,* **56,** 2–20.

——, A. B. White, and S. K. Avery, 1994: Boundary-layer depth and entrainment zone characterization with a boundary-layer profiler. *Bound.-Layer Meteor.,* **68,** 375–385.

——, H. K. Baltink, and F. C. Bosveld, 2001: Observations of the morning transition of the convective boundary layer. *Bound.-Layer Meteor.,* **101,** 209–227.

Antikainen, V., A. Paukkunen, and H. Jauhiainen, 2002: Measurement accuracy and repeatability of Vaisala RS90 radiosonde. *Vaisala News,* No. 159, Vaisala Oyj, Helsinki, Finland, 11–13.

Atkinson, B. W., and J. W. Zhang, 1996: Mesoscale shallow convection in the atmosphere. *Rev. Geophys.,* **34,** 403–431.

Boers, R., and E. W. Eloranta, 1986: Lidar measurements of the atmospheric entrainment zone and the potential temperature jump across the mixed layer. *Bound.-Layer Meteor.,* **34,** 357–375.

Bruneau, D., P. Quaglia, C. Flamant, M. Meissonier, and J. Pelon, 2001: Airborne lidar LEANDRE II for water-vapor profiling in the troposphere. *Appl. Opt.,* **40,** 3450–3475.

Cohn, S. A., and W. M. Angevine, 2000: Boundary-layer height and entrainment zone thickness measured by lidars and wind profiling radars. *J. Appl. Meteor.,* **39,** 1233–1247.

Couvreux, F., F. Guichard, J. L. Redelsperger, C. Kiemle, V. Masson, J. P. Lafore, and C. Flamant, 2005: Water-vapour variability within a convective boundary-layer assessed by large-eddy simulations and IHOP_2002 observations. *Quart. J. Roy. Meteor. Soc.,* **131,** 2665–2693.

——, ——, V. Masson, and J. Redelsperger, 2007: Negative water vapour skewness and dry tongues in the convective boundary layer: observations and large-eddy simulation budget analysis. *Bound.-Layer Meteor.,* **123,** 269–294.

——, ——, P. H. Austin, and F. Chen, 2009: Nature of the mesoscale boundary layer height and water vapor variability observed 14 June 2002 during the IHOP_2002 campaign. *Mon. Wea. Rev.,* **137,** 414–432.

Crook, N. A., 1996: Sensitivity of moist convection forced by boundary layer processes to low-level thermodynamic fields. *Mon. Wea. Rev.,* **124,** 1767–1785.

Crum, T. D., R. B. Stull, and E. W. Eloranta, 1987: Coincident lidar and aircraft observations of entrainment into thermals and mixed layers. *J. Climate Appl. Meteor.,* **26,** 774–788.

Davis, K. J., N. Gamage, C. R. Hagelberg, C. Kiemle, D. H. Lenschow, and P. P. Sullivan, 2000: An objective method for deriving atmospheric structure from airborne lidar observations. *J. Atmos. Oceanic Technol.,* **17,** 1455–1468.

Dodd, A. V., 1965: Dew point distribution in the contiguous United States. *Mon. Wea. Rev.,* **93,** 113–122.

Emeis, S., K. Schafer, and C. Munkel, 2008: Surface-based remote sensing of the mixing-layer height—A review. *Meteor. Z.,* **17,** 621–630.

Garratt, J. R., 1994: *The Atmospheric Boundary Layer*. Cambridge University Press, 316 pp.

Geerts, B., and Q. Miao, 2005: The use of millimeter Doppler radar echoes to estimate vertical air velocities in the fair-weather convective boundary layer. *J. Atmos. Oceanic Technol.,* **22,** 225–246.

Grossman, R. L., and N. Gamage, 1995: Moisture flux and mixing processes in the daytime continental convective boundary layer. *J. Geophys. Res.,* **100** (D12), 25 665–25 674.

Hardy, K. R., and H. Ottersten, 1969: Radar investigation of convective patterns in the clear atmosphere. *J. Atmos. Sci.,* **26,** 666–672.

Harper, W. G., F. H. Ludlam, and P. M. Saunders, 1957: Radar echoes from cumulus clouds. *Proc. Sixth Weather Radar Conf.,* Cambridge, MA, Amer. Meteor. Soc., 267–272.

Hoch, J., and P. Markowski, 2005: A climatology of springtime dryline position in the U.S. Great Plains region. *J. Climate,* **18,** 2132–2137.

Ince, T., S. J. Frasier, A. Muschinksi, and A. L. Pazmany, 2003: An S-band frequency-modulated continuous-wave boundary layer profiler: Description and initial results. *Radio Sci.,* **38,** 1072, doi:10.1029/2002RS002753.

Knupp, K. R., 2006: Observational analysis of a gust front to bore to solitary wave transition within an evolving nocturnal boundary layer. *J. Atmos. Sci.,* **63,** 2016–2035.

Konrad, T. G., 1970: The dynamics of the convective process in clear air as seen by radar. *J. Atmos. Sci.,* **27,** 1138–1147.

Lapworth, A., 2006: The morning transition of the nocturnal boundary layer. *Bound.-Layer Meteor.,* **119,** 501–526.

LeMone, M. A., and W. T. Pennell, 1976: The relationship of trade wind cumulus distribution to subcloud layer fluxes and structure. *Mon. Wea. Rev.,* **104,** 524–539.

——, and Coauthors, 2002: CASES-97: Late-morning warming and moistening of the convective boundary layer over the Walnut River watershed. *Bound.-Layer Meteor.,* **104,** 1–52.

Lin, Y.-L., 2007: *Mesoscale Dynamics*. Cambridge University Press, 674 pp.

Linne, H., B. Hennemuth, J. Bosenberg, and K. Ertel, 2007: Water vapour flux profiles in the convective boundary layer. *Theor. Appl. Climatol.,* **87,** 201–211.

Mahrt, L., 1976: Mixed layer moisture structure. *Mon. Wea. Rev.,* **104,** 1403–1407.

——, 1979: An observational study of the structure of the nocturnal boundary layer. *Bound.-Layer Meteor.,* **17,** 247–264.

——, 1991: Boundary-layer moisture regimes. *Quart. J. Roy. Meteor. Soc.,* **117,** 151–176.

Miao, Q., B. Geerts, and M. LeMone, 2006: Vertical velocity and buoyancy characteristics of coherent echo plumes in the convective boundary layer, detected by a profiling airborne radar. *J. Appl. Meteor. Climatol.,* **45,** 838–855.

Pazmany, A., R. McIntosh, R. Kelly, and G. Vali, 1994: An airborne 95 GHz dual-polarized radar for cloud studies. *IEEE Trans. Geosci. Remote Sens.,* **32,** 731–739.

Perry, K. D., and P. V. Hobbs, 1996: Influences of isolated cumulus clouds on the humidity of their surroundings. *J. Atmos. Sci.,* **53,** 159–174.

Schwemmer, G. K., 1998: Holographic airborne rotating lidar instrument experiment (HARLIE). Extended Abstracts, *19th Int. Laser Radar Conf.,* Annapolis, MD, NASA, 623–626.

Seibert, P., F. Beyrich, S. Gryning, S. Joffre, A. Rasmussen, and P. Tercier, 2000: Review and intercomparison of operational methods for the determination of the mixing height. *Atmos. Environ.,* **34,** 1001–1027.

Stull, R. B., 1988: *An Introduction to Boundary Layer Meteorology*. Kluwer Academic, 666 pp.

Warner, J., and J. W. Telford, 1963: Some patterns of convection in the lower atmosphere. *J. Atmos. Sci.,* **20,** 313–318.

——, and ——, 1967: Convection below cloud base. *J. Atmos. Sci.,* **24,** 374–382.

Weckwerth, T. M., 2000: The effect of small-scale moisture variability on thunderstorm initiation. *Mon. Wea. Rev.,* **128,** 4017–4030.

——, J. W. Wilson, and R. M. Wakimoto, 1996: Thermodynamic variability within the convective boundary layer due to horizontal convective rolls. *Mon. Wea. Rev.,* **124,** 769–784.

——, T. W. Horst, and J. W. Wilson, 1999: An observational study of the evolution of horizontal convective rolls. *Mon. Wea. Rev.,* **127,** 2160–2179.

——, and Coauthors, 2004: An overview of the International H_2O Project (IHOP_2002) and some preliminary highlights. *Bull. Amer. Meteor. Soc.,* **85,** 253–277.

White, A. B., C. W. Fairall, and D. W. Thomson, 1991: Radar observations of humidity variability in and above the marine atmospheric boundary layer. *J. Atmos. Oceanic Technol.,* **8,** 639–658.

Whiteman, D. N., and S. H. Melfi, 1999: Cloud liquid water, mean droplet radius, and number density measurements using a raman lidar. *J. Geophys. Res.,* **104** (D24), 31 411–31 419.

——, ——, and R. A. Ferrare, 1992: Raman lidar system for the measurement of water vapor and aerosols in the Earth's atmosphere. *Appl. Opt.,* **31,** 3068–3082.

Wilson, J. W., T. M. Weckwerth, J. Vivekanandan, R. M. Wakimoto, and R. W. Russell, 1994: Boundary layer clear-air radar echoes: Origin of echoes and accuracy of derived winds. *J. Atmos. Oceanic Technol.,* **11,** 1184–1206.

Wurman, J., J. Straka, E. Rasmussen, M. Randall, and A. Zahrai, 1997: Design and deployment of a portable, pencil-beam, pulsed, 3-cm Doppler radar. *J. Atmos. Oceanic Technol.,* **14,** 1502–1512.

Wyngaard, J. C., and M. LeMone, 1980: Behaviour of the refractive index structure parameter in the entraining convective boundary layer. *J. Atmos. Sci.,* **37,** 1573–1585.